



Cite this: *Phys. Chem. Chem. Phys.*,  
2018, **20**, 17799

## Anharmonic contribution to the stabilization of $\text{Mg(OH)}_2$ from first principles

P. Treviño,<sup>\*a</sup> A. C. García-Castro,<sup>bc</sup> S. López-Moreno,<sup>id</sup> \*d A. Bautista-Hernández,<sup>ID</sup><sup>e</sup> E. Bobociovu,<sup>f</sup> B. Reynard,<sup>f</sup> R. Caracas<sup>f</sup> and A. H. Romero<sup>ID</sup><sup>eg</sup>

Geometrical and vibrational characterization of magnesium hydroxide was performed using density functional theory. Four possible crystal symmetries were explored:  $P\bar{3}$  (No. 147, point group  $-3$ ),  $C2/m$  (No. 12, point group  $2$ ),  $P\bar{3}m1$  (No. 156, point group  $3m$ ) and  $P\bar{3}m1$  (No. 164, point group  $-3m$ ) which are the currently accepted geometries found in the literature. While a lot of work has been performed on  $\text{Mg(OH)}_2$ , in particular for the  $P\bar{3}m1$  phase, there is still a debate on the observed ground state crystal structure and the anharmonic effects of the OH vibrations on the stabilization of the crystal structure. In particular, the stable positions of hydrogen are not yet defined precisely, which have implications in the crystal symmetry, the vibrational excitations, and the thermal stability. Previous work has assigned the  $P\bar{3}m1$  polymorph as the low energy phase, but it has also proposed that hydrogens are disordered and they could move from their symmetric position in the  $P\bar{3}m1$  structure towards  $P\bar{3}$ . In this paper, we examine the stability of the proposed phases by using different descriptors. We compare the XRD patterns with reported experimental results, and a fair agreement is found. While harmonic vibrational analysis shows that most phases have imaginary modes at 0 K, anharmonic vibrational analysis indicates that at room temperature only the  $C2/m$  phase is stabilized, whereas at higher temperatures, other phases become thermally competitive.

Received 18th April 2018,  
Accepted 1st June 2018

DOI: 10.1039/c8cp02490a

rsc.li/pccp

### 1 Introduction

Magnesium hydroxide ( $\text{Mg(OH)}_2$ ), also called brucite, is a mineral widely used as a medical and industrial product of many different reactions. For example,  $\text{Mg(OH)}_2$  is commonly used as a flame retardant filler in composite materials because of its ability to undergo endothermic dehydration in fire conditions.<sup>1,2</sup> In recent research, it has been found that  $\text{Mg(OH)}_2$  can be used as starting material for controlling the synthesis of nanoscale magnesium oxide ( $\text{MgO}$ ), where the crystallite size and morphological features of  $\text{Mg(OH)}_2$  can be well-retained.<sup>3</sup>

The crystal structure is based on a structurally bound Mg–OH skeleton arranged in a hexagonal pattern. The resulting sheets of  $\text{Mg(OH)}_6$  octahedra constitute the main building unit as in many other layered hydrous minerals. Its structure was first established by Zigan and Rothbauer (1967),<sup>4</sup> it crystallizes in the  $P\bar{3}m1$  space group with a Mg atom at the 1a (0, 0, 0) Wyckoff position while O and H atoms are at 2d (1/3, 2/3, z). Each OH dipole faces three opposite symmetrical hydroxyl groups from the neighboring layer: the H–H interlayer distance is 1.97 Å, and the width of the layers is 3.15 Å.

This compound represents an exciting example of systems with different kinds of bonds: Mg–O is ionic, O–H has a strong covalent character, and the interlayer interaction is weak and mainly dispersive, with a small electrostatic contribution.<sup>5,6</sup>

$\text{Mg(OH)}_2$  has been extensively investigated by experimental techniques such as neutron diffraction, Raman and infrared spectroscopies and NMR.<sup>7–12</sup> These studies suggest that the interlayer bonding is weak and mainly associated with dispersion-type forces. Since the latter are directly linked to electron correlation, modeling them with normal exchange–correlation functionals represents a difficult task.<sup>5</sup> Despite its simple structure, a full description of its physical properties remain unexplored; even its crystallographic symmetry has not yet been fully established. Although the question of its structure has been addressed several times in the past,<sup>8,13–16</sup> the models

<sup>a</sup> Centro de Investigación y Estudios Avanzados del IPN, MX-76230, Querétaro, Mexico. E-mail: polivia@ciinvestav.mx

<sup>b</sup> Physique Théorique des Matériaux, Université de Liège, B-4000 Sart-Tilman, Belgium

<sup>c</sup> Departamento de Física, Universidad Industrial de Santander, Cra 27 Cl 9, Bucaramanga, Colombia

<sup>d</sup> CONACYT – División de Materiales Avanzados, IPICYT, Camino a la presa San José 2055, San Luis Potosí, SLP. 78216, Mexico.

E-mail: sinhue.lopez@ipicyt.edu.mx

<sup>e</sup> Facultad de Ingeniería, Benemérita Universidad Autónoma de Puebla, Apdo. Postal J-39, Puebla, Pue. 72570, Mexico

<sup>f</sup> CNRS, Laboratoire de Géologie de Lyon UMR CNRS 5276, Ecole Normale Supérieure de Lyon, Site Monod, 46 allé d’Italie, 69364 Lyon Cedex 07, France

<sup>g</sup> Physics Department, West Virginia University, WV-26506-6315, Morgantown, USA

proposed previously deal with temporally and spatially averaged positions of the hydrogen subsystem and suggest that hydrogen atoms are in fact displaced from the high-symmetry points on the three-fold axis to form a new lattice with  $P\bar{3}$  symmetry and an averaged 1/3 occupancy of three equivalent 6i Wyckoff positions ( $x, 2x, z$ ) with either  $x > 1/3$  (the so-called XGT arrangement) or  $x < 1/3$  (the so-called XLT arrangement).<sup>16</sup> The case for the XGT arrangement is further strengthened by the neutron diffraction experiments of Desgranges *et al.*<sup>7</sup> indicating that protons are displaced into XGT positions even at ambient pressure.<sup>13</sup>

Neutron diffraction experiments show that the average hydrogen position does not coincide with the threefold axis at high pressures, but splits into three symmetrically equivalent off-axis positions. To capture these transitions, when hydrogen atoms are permitted to occupy 6i-like positions, the resulting space group is  $P\bar{3}$  (a maximal subgroup of  $P\bar{3}m1$ ), with the loss of the mirror planes as the protons are disordered spatially.<sup>16</sup> The resulting  $P\bar{3}$  structure has lower energy than the  $P\bar{3}m1$  structure.

Jochym *et al.*<sup>13</sup> observed that the positions of the hydrogen atoms around the three-fold axis were not well constrained in the system, *i.e.*, they probably move in a very shallow potential well. This observation is in concordance with previous experimental evidence.<sup>11</sup> It suggests that the structure of the magnesium hydroxide crystal may be more complicated than is currently accepted. The examination of the MD trajectories shows large amplitude hydrogen movements even for runs performed at low temperature.<sup>13</sup> They observed that the lattice lock-in still appeared to be present at 244 K, but hydrogen atoms do not spend most of their time in the vicinity of their high-symmetry positions.

According to previous approximations, we performed an analysis over possible crystal structures that are related by symmetry and could mimic the proton displacement on top of the Mg sublattice:  $C2/m$ ,  $P\bar{3}m1$ ,  $P3m1$  and  $P\bar{3}$ .

The present work is organized as follows. In Section 2 we give a detailed description of the experimental and computational methods used in this paper. The results and discussion of the structural optimization and the simulated XRD patterns are in Section 3.1. In Section 3.2 the harmonic thermal analysis is presented, while the anharmonic vibrational analysis is in Section 3.3. Finally, we discuss and summarize the primary results of this work in Section 4.

## 2 Computational and experimental details

In order to understand the real structure of brucite, four systems were compared:  $P\bar{3}m1$ ,  $P3m1$ ,  $P\bar{3}$  and  $C2/m$ , see Fig. 1. The first-principles calculations have been performed within Density Functional Theory (DFT) as implemented in the Vienna Ab initio Simulation Package (VASP)<sup>17,18</sup> with the Projector Augmented Wave (PAW) formulation.<sup>19</sup> The valence electron configurations taken into account in the atomic pseudo-potential were: Mg (3s<sup>2</sup>), O (2s<sup>2</sup>2p<sup>4</sup>) and H (1s<sup>1</sup>). We used the General Gradient Approximation (GGA) to express the exchange-correlation

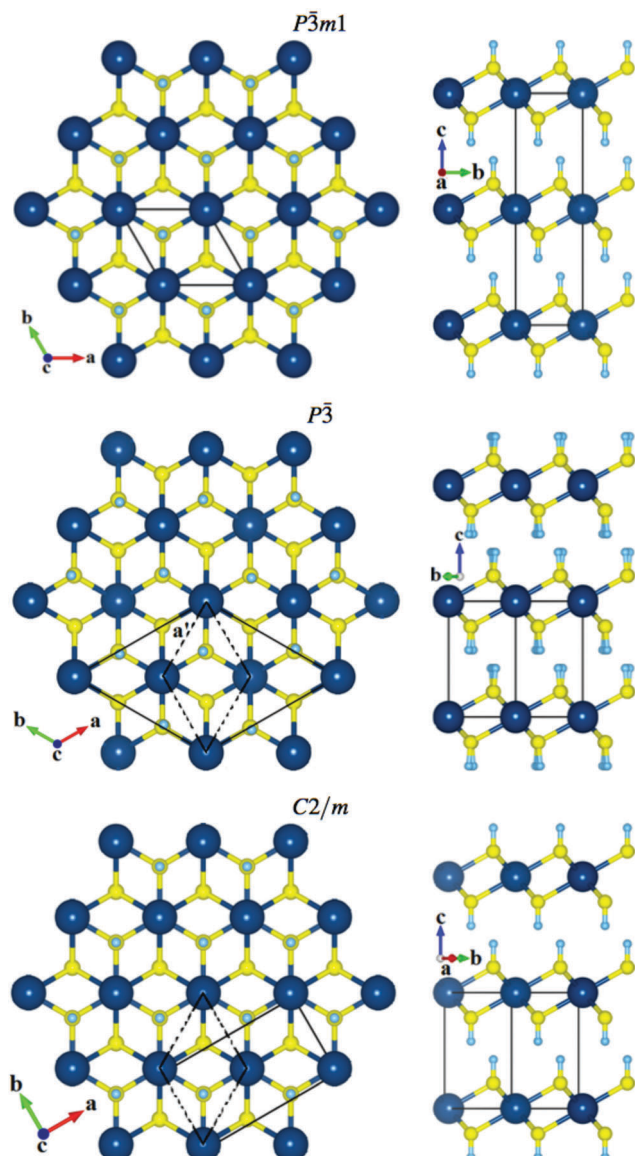


Fig. 1 Proposed structures for brucite:  $P\bar{3}m1$ ,  $P\bar{3}$  and  $C2/m$  symmetries. The equivalent cell parameters are shown with dashed lines. Mg, O, and H are in blue, yellow, and cyan colors.

functional with the Perdew–Burke–Ernzerhof for Solids (PBEsol) parametrization.<sup>20</sup> The reciprocal space integration for the unit cell was carried out over the set of  $k$ -points  $9 \times 9 \times 3$  generated according to the Monkhorst–Pack scheme.<sup>21</sup> An energy cut-off of 550 eV was used to achieve a residual error on the forces of less than 1 meV Å<sup>-1</sup> after the full convergence test. The electronic structure was computed with a higher set of  $k$ -points. Vibrational properties were computed through the formalism of density functional perturbation theory (DFPT),<sup>22</sup> and postprocessing analysis was carried out with the Phonopy code<sup>23</sup> and PHONON.<sup>24</sup> The last program has been used with success in the study of the vibrational properties of other AX<sub>2</sub> compounds such as MnF<sub>2</sub>,<sup>25</sup> FeF<sub>2</sub>,<sup>26</sup> and CoF<sub>2</sub>.<sup>27</sup> The interatomic constants were computed on a high-symmetry grid of  $k$  points, obtained from a  $3 \times 3 \times 1$  supercell.

Theoretical Raman spectra were obtained by computing the Raman tensors, *i.e.*, the change in dielectric tensor due to the atomic displacement occurring during a given vibration. The computations were realized using DFPT<sup>22,28</sup> as implemented in the ABINIT package,<sup>29–31</sup> with norm-conserving Troullier–Martins-type pseudopotentials<sup>32</sup> in the local density approximation. More details of the calculations, including the crystal structures, the normal modes and their atomic displacement patterns can be found on the WURM website.<sup>33</sup>

The high-temperature anharmonicity of Mg(OH)<sub>2</sub> was described using *ab initio* molecular dynamics in combination with the temperature dependent effective potential technique (TDEP),<sup>34,35</sup> where the effective interatomic force constants are fitted to a harmonic potential at finite temperature. The fitted model is used to obtain higher order terms in the energy with respect to the atomic displacements, which are then used to calculate the thermal conductivity (see ref. 34 and 35 for details). The simulation cell was constructed from a 3 × 3 × 1 repetition of the unit cell (80, 120, 90, and 90 atoms for C2/m, P $\bar{3}$ , P3m1, and P $\bar{3}$ m1, respectively). The molecular dynamics was run at 300 and 600 K using a 3 × 3 × 1 mesh to perform any Brillouin zone integration and an energy cutoff of 550 eV for about 4000-time steps with a one fs time step. The temperature was controlled with a Nose–Hoover thermostat.<sup>36,37</sup>

The Raman measurements were performed at liquid nitrogen temperature with a confocal LabRam HR DILOR microspectrometer equipped with 1800 g mm<sup>-1</sup> gratings and using the 514.53 nm line of a Spectra-Physics Ar<sup>+</sup> laser for excitation.<sup>38</sup>

## 3 Results and discussion

### 3.1 Structural optimization

C2/m corresponds to the lowest energy configuration, almost degenerate with P $\bar{3}$ m1 and P $\bar{3}$  (with energy differences smaller than 0.005 eV per f.u.) but with an energy difference of 1.2 eV per f.u. with respect to P3m1. That indicates that P3m1 is not even energetically competitive with the other phases, and we will not consider it in our discussion below.

Table 1 compares our results with previous values published in the literature. Among these approaches, several codes have been used, *e.g.*, CRYSTAL and VASP, with different Hamiltonians and different approximations, and all of them present good agreement with experimental cell parameters.<sup>5,6,16</sup>

After the structural relaxation, we obtained the lattice parameters:  $a = 3.1877 \text{ \AA}$  and  $c = 4.786 \text{ \AA}$  for the P $\bar{3}$ m1 structure. Even when  $a$  and  $c$  are overestimated, our cell parameters are in good agreement with experimental results ( $a = 3.142 \text{ \AA}$  and  $c = 4.766 \text{ \AA}$ );  $a$  differs by 1.45% and  $c$  differs by 0.4% with respect to the experimental parameters of Zigan and Rothbauer.<sup>4</sup> The calculated equilibrium volume presents an overestimation of 3%.

Even when structures P $\bar{3}$ m1 and P $\bar{3}$  are very similar (see Fig. 1), their unit cells are different. So, it is necessary to establish equivalent parameters to compare results. Both structures have a hexagonal arrangement for the Mg cations surrounded by the hydroxyls, where three of them are oppositely oriented to the three

**Table 1** Lattice parameters of Mg(OH)<sub>2</sub> obtained in this work (results with PBEsol) and the experimental and theoretical results reported from the literature, where the labels used have the following meaning: XD: X-ray diffraction; ND: neutron diffraction; HF: Hartree–Fock; B3LYP: Becke 3-parameter Lee–Yang–Parr; VWN: Vosko–Wilk–Nusair; LDA: local density approximation; PW: Perdew Wang; PBE: Perdew–Buerke–Ernzerhof; PBEsol: PBE for solids; HSE06: Heyd–Scuseria–Ernzerhof

	$a$ (Å)	$c$ (Å)	$c/a$	$V_0$ (Å <sup>3</sup> )	Method	Ref.
$P\bar{3}m1$	3.146	4.769	1.516	40.88	XD	39
	3.149	4.749	1.508	40.78	XD	40
	3.147	4.770	1.516	40.92	XD	41
	3.140	4.760	1.516	40.80	XD	42
	3.138	4.713	1.502	40.20	ND	8
	3.150	4.770	1.498	40.56	ND	12
	3.142	4.766	1.517	40.75	ND	4
	3.148	4.779	1.518	41.01	ND	7
	3.161	4.696	1.486	40.64	HF	43
	3.152	5.185	1.645	44.61	HF	5
	3.148	5.263	1.672	45.20	HF	6
	3.167	4.854	1.533	42.20	B3LYP	6
	3.172	4.892	1.542	42.63	B3LYP	5
	3.087	4.470	1.448	36.89	VWN	5
	3.000	4.570	1.523	35.61	LDA	44
	3.099	4.413	1.424	36.70	LDA	6
	3.175	4.662	1.468	40.70	PW	5
	3.142	4.766	1.517	40.75	PW91	45
	3.179	4.717	1.484	41.30	PW91	6
	3.180	4.763	1.498	41.70	PW91	46
	3.116	4.823	1.548	40.55	PBE	38
	3.189	4.773	1.497	42.02	PBE	47
	3.182	4.801	1.509	42.10	PBE	48
	3.126	4.730	1.513	40.04	HSE06	47
	3.188	4.786	1.501	42.12	PBEsol	
$P\bar{3}$	3.186	4.777	1.499	42.00	PBEsol	
	3.188	4.780	1.499	42.07	PBEsol	
$C2/m$	3.188	4.780	1.499	42.07	PBEsol	

hydroxyls of the next layer. For both structures, the interlayer distance is the same since Mg cations maintain their general positions, even when there is a slight up and down deviation from the original position. Therefore, in the case of the  $c$  parameter, both values are the same, and they can be compared directly.

This is not the case for the  $a$  lattice parameter because the unit cell of the P $\bar{3}$  structure is larger than the P $\bar{3}$ m1 one. In the P $\bar{3}$  structure, the hydrogen ions begin to deviate from their initial position as if they were rotating. This rotation expands the unit cell and preserves the symmetry. To compare the  $a$  lattice parameter, we consider the distance between the first in-plane Mg–Mg neighbors as shown in Fig. 1. This equivalent  $a$  parameter will be designated as  $a'$  and it can be calculated as follows:  $a' = a_{P\bar{3}}/(2 \cos 30)$ .

After the structural relaxation, the obtained lattice parameters of the P $\bar{3}$  system were:  $a = 5.518 \text{ \AA}$  and  $c = 4.777 \text{ \AA}$  with  $a' = 3.186 \text{ \AA}$ . This  $a'$  parameter is shown in Table 1. Both values are overestimated, but they are in good agreement with the experimental parameters;  $a$  differs by 1.4% and  $c$  differs by 0.2%. The difference between the  $a$  parameter for the P $\bar{3}$ m1 structure and the  $a'$  parameter for P $\bar{3}$  is just 0.05%, and the difference for the  $c$  parameter is just 0.19%. For the C2/m system, we obtained the values  $a = 3.188 \text{ \AA}$  and  $c = 4.780 \text{ \AA}$ , which are in good agreement with experimental values;  $a$  is overestimated by 1.4% and  $c$  is overestimated by 0.08%. The difference between the  $a$  parameter for the P $\bar{3}$ m1 structure and

the  $a$  parameter for  $C2/m$  is 0.003%, and the difference for the  $c$  parameter is 0.3%. In  $C2/m$ , the Mg, O, and H atoms are located in the 2a (0, 0, 0), 4i (0.6667, 0, 0.2180), and 4i (0.6666, 0, 0.4212) Wyckoff positions, respectively.

Fig. 2 shows simulated XRD patterns with  $K\alpha$ :Cu for the three structures. As the position of H is invisible to XRD due to its low scattering factor, all the computed XRD patterns yield similar results, omitting the order-disorder character. The only small differences between the various patterns come from different intra-layer and interlayer dimensions. However, such measurements are not necessarily sensitive enough to distinguish between the three theoretical variants proposed here.

Regarding the electronic structure of magnesium hydroxide, it is well known that  $Mg(OH)_2$  is a direct bandgap material, *i.e.*, both the valence band (VB) maximum and the conduction band (CB) minimum are located at the  $\Gamma$  point. This feature can be observed in the electronic band structure of Fig. 3(a). Previous theoretical studies of the hexagonal  $P\bar{3}m1$  phase of  $Mg(OH)_2$  reported different band-gap values depending on the exchange-correlation functional used.<sup>47,49</sup> On one side, in ref. 47 a gap value of 4.2 (7.7) eV was reported obtained with the PBE (HSE06) exchange-correlation functional. In that work, it was

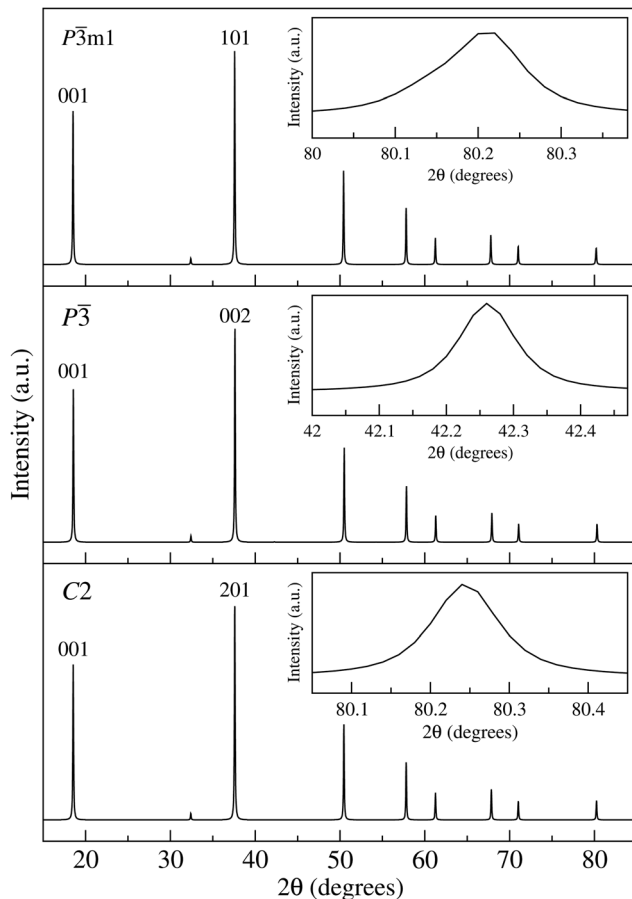


Fig. 2 Simulated XRD patterns for the  $P\bar{3}m1$ ,  $P\bar{3}$  and  $C2/m$  symmetries. It can be observed that the characteristic peaks for  $P\bar{3}m1$  are located at the same angles as those of  $P\bar{3}$  and  $C2/m$ . This was expected because the only difference between them consists of the rotated position of H atoms.

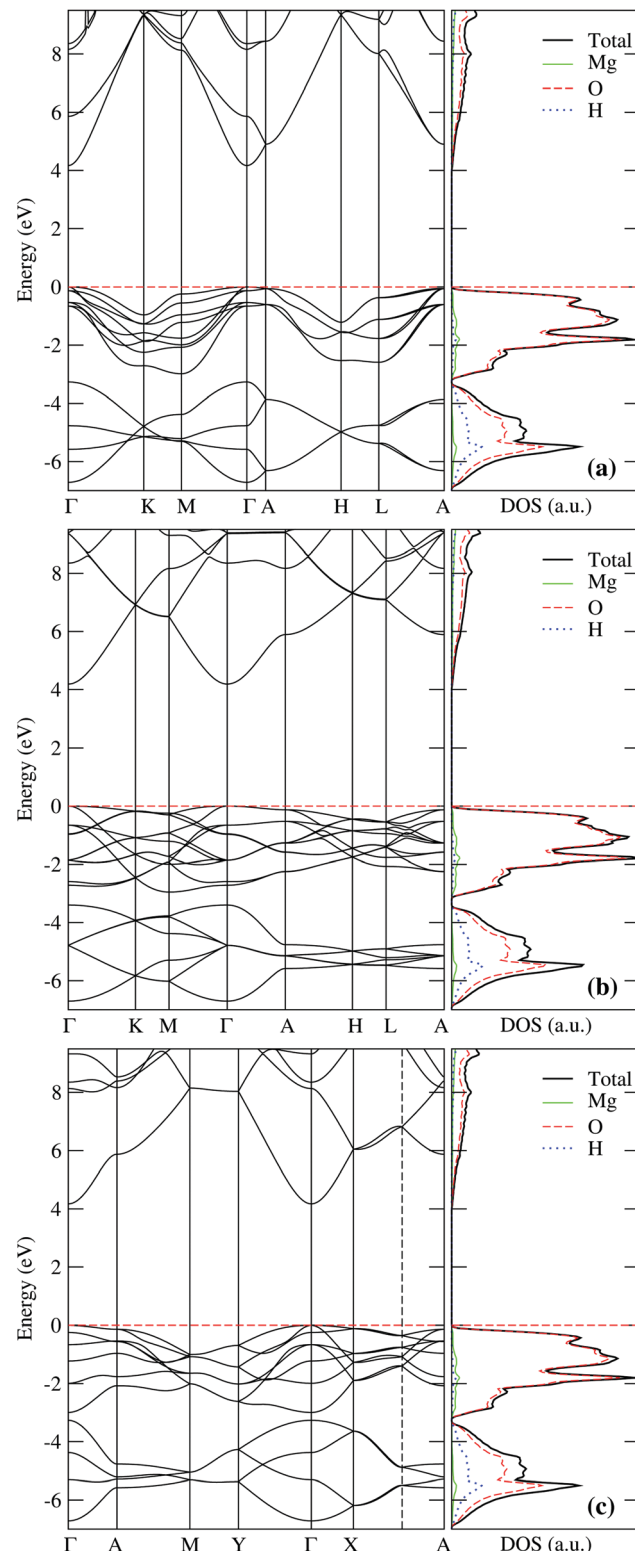


Fig. 3 Electronic band structure and total density of states (DOS) for (a)  $P\bar{3}m1$ , (b)  $P\bar{3}$ , and (c)  $C2/m$  symmetries.

determined that valence and conduction bands obtained with both functionals have a similar dispersion and curvature. So, no matter if the calculations are performed at the level of GGA

or hybrid functionals, the dispersion and the general features of the band structure, except for the band gap value, are well represented with both functionals. According to our results, the band gap value for the three polymorphs is around 4.18 eV, Fig. 3(a)–(c). As can be seen, the total and partial density of states from the three phases are very similar, where the zone from  $-3$  to the Fermi level is mainly occupied by  $2p_x$  and  $2p_y$  states from O with fewer contributions from  $2p_z$  states. In this zone, there are also states from s orbitals, mainly from Mg with minor contributions from O and H, while the zone from  $-3$  to  $-7$  eV is filled with  $2p$  states from O (mostly  $2p_z$ ) and s states from H and Mg. Deeper states at  $-18$  eV are due to s states, mainly from O with minor contributions from H and Mg, whereas the bands from  $4$  to  $10$  eV are filled mainly by O ( $2p_z$  and  $2s$ ) with minor contributions from s orbitals from Mg.

For the  $P\bar{3}m1$  phase, the VB maximum is occupied mostly by O ( $2p_x$  and  $2p_y$  states) with a small contribution from Mg ( $2s$  states). The CB minimum is filled almost by O  $2s$  states with a small part from Mg  $2s$  states and a minimal contribution from H  $1s$  states. In general, the occupation of the VB maximum and CB minimum from the other two phases is similar to the  $P\bar{3}m1$  one. The most significant difference is that in the  $P\bar{3}$  and  $C2/m$  phases, small contributions to the VB maximum appear from  $2p_z$  states from O. More significant changes are observed at deeper energy levels, mainly in those cases where a specific orbital has a small contribution in a range of energy.

### 3.2 Harmonic thermal analysis (phonons)

Group theory predicts that the brucite structure (space group  $P\bar{3}m1$  and five atoms in the unit cell) has the following phonon mode representation at the  $\Gamma$  point:  $\Gamma = 2A_{1g} + 3A_{2u} + 2E_g + 3E_u$ ,<sup>38</sup> where the acoustic modes are one  $A_{2u}$  and one  $E_u$ . The structure possesses a center of inversion, and the rule of mutual exclusion leads to there being four symmetric g-modes which are Raman active and four antisymmetric u-modes which are infrared active. Since the Mg ions are located at the centers of inversion, they do not take part in any of the Raman active g-modes whose normal coordinates are symmetric with respect to the inversion symmetry operation,<sup>50</sup> but they participate in the 'u' motions, in order to preserve the center of the mass structure.

According to Lutz,<sup>51</sup> three kind of modes involving the H atoms can be distinguished when dealing with a system such as brucite: OH translation, OH libration (commonly referred to as hydrogen bending in a molecular context) and OH stretching. Translational modes that correspond to vibrations of the O–H units can be either parallel ( $A_{1g}(T)$  and  $A_{2u}(T)$ ) or perpendicular ( $E_g(T)$  and  $E_u(T)$ ) to the  $c$  axis. The rotational vibrations of the OH ions are:  $E_g(R)$  and  $E_u(R)$ . The internal modes are symmetric and antisymmetric O–H stretching vibrations ( $A_{1g}(I)$  and  $A_{2u}(I)$ ).<sup>9</sup>

According to our results, all Raman and infrared active modes of brucite were detected (see Table 2) and they are in good agreement with previous experimental data.<sup>50</sup> But it should be pointed out that there are some differences in the band positions of brucite reported in the literature. This occurs because brucite is characterized by weak infrared absorption

**Table 2** Calculated and previous reported<sup>6,38,50</sup> Raman (R) and infrared (IR) active modes from the  $P\bar{3}m1$  phase, and the present results from the  $P\bar{3}$  and  $C2/m$  phases

Mode	Exp. <sup>50</sup>	Ref. 6	Ref. 38	Computed		
				$P\bar{3}m1$	$P\bar{3}$	$C2/m$
R	280	278	268	267.6 (E <sub>g</sub> )	267.0 (2A <sub>g</sub> )	267.8 (B <sub>g</sub> )
IR					275.1 (A <sub>u</sub> )	
R					280.0 (A <sub>g</sub> )	268.0 (A <sub>g</sub> )
IR					332.6 (A <sub>u</sub> )	
R					333.5 (A <sub>g</sub> )	
IR(TO)	361	364	349	352.2 (E <sub>u</sub> )	338.1 (A <sub>u</sub> )	352.1 (A <sub>u</sub> )
IR(LO)			375			
IR						352.4 (B <sub>u</sub> )
R					411.2 (A <sub>g</sub> )	
IR(TO)	416	459	422	426.2 (E <sub>u</sub> )	431.3 (A <sub>u</sub> )	425.9 (A <sub>u</sub> )
IR(LO)			727			
IR						426.3 (B <sub>u</sub> )
R	443	454	449	435.2 (A <sub>1g</sub> )	445.6 (A <sub>g</sub> )	435.5 (A <sub>g</sub> )
IR(TO)	461	499	487	471.1 (A <sub>2u</sub> )	470.4 (A <sub>u</sub> )	471.0 (B <sub>u</sub> )
IR(LO)			600			
R					693.5 (A <sub>g</sub> )	
IR					722.3 (A <sub>u</sub> )	
R	725	803	767	786.3 (E <sub>g</sub> )	812.5 (A <sub>g</sub> )	788.2 (A <sub>g</sub> )
R					956.6 (A <sub>g</sub> )	788.4 (B <sub>g</sub> )
IR					961.4 (A <sub>u</sub> )	
R	3652	3847	3686	3726.8 (A <sub>1g</sub> )	3722.0 (A <sub>g</sub> )	3726.2 (A <sub>g</sub> )
IR					3733.2 (2A <sub>u</sub> )	
R					3733.7 (2A <sub>g</sub> )	
IR(TO)	3688	3873	3727	3769.3 (A <sub>2u</sub> )	3765.2 (A <sub>u</sub> )	3768.9 (B <sub>u</sub> )
IR(LO)			3741			

and emission bands that are easily masked by the presence of impurities such as talc, calcite, and serpentine. Even when XRD does not observe some of these impurities, they easily affect the infrared emission spectra.<sup>52</sup>

The calculated phonons correspond to the E<sub>g</sub> mode at  $268\text{ cm}^{-1}$  (OH group displacements in the (001) plane), the E<sub>g</sub>(R) mode at  $786\text{ cm}^{-1}$  (rocking motion of a H atom), the A<sub>1g</sub> mode at  $435\text{ cm}^{-1}$  (a breathing mode), the high frequency A<sub>1g</sub> mode at  $3726\text{ cm}^{-1}$ , E<sub>u</sub> modes at  $352$  and  $426\text{ cm}^{-1}$  (H atom displacements parallel to the basal plane), the A<sub>2u</sub> mode at  $471\text{ cm}^{-1}$  (vibration of the Mg sub lattice), and the A<sub>2u</sub> mode at  $3769\text{ cm}^{-1}$  (an OH stretching mode). A more clear description of the assignation of modes is given in ref. 38.

The computed frequency for the stretching mode of an isolated hydroxyl group is  $3769\text{ cm}^{-1}$  which lies just  $81\text{ cm}^{-1}$  above the experimental value,<sup>46</sup> which corresponds to a crystal-induced substantial OH frequency shift. The A<sub>1g</sub>–A<sub>2u</sub> splitting is  $36\text{ cm}^{-1}$ , in agreement with experimental reports. If there is a transition involving rearrangements of the H atoms, it should be consistent with both the Raman and the diffraction data.<sup>9</sup> Neutron diffraction of brucite was carried out by Catti *et al.* and Parise *et al.*<sup>8,12</sup> They obtained improved fits for models in which the H or D atoms that move away from the threefold axis are split over three sites corresponding to the positions of the O atoms. There is also evidence for long-range disordering of the H sublattice at ambient pressure in divalent metal hydroxides like Ca(OH)<sub>2</sub>,<sup>7</sup> where the H atoms can be modeled as being dynamically disordered among three equivalent positions at  $10^\circ$  from the  $c$  axis at room temperature.

Brucite with  $P\bar{3}$  structure, with 15 atoms in the unit cell, has 45 normal modes. According to group theory, the acoustic modes are  $A_u$ ,  $^1E_u$  and  $^2E_u$ . Six modes are infrared active ( $2A_u$ ,  $2^1E_u$  and  $2^2E_u$ ) and three modes are Raman active ( $A_g$ ,  $^1E_g$  and  $^2E_g$ ). Table 2 shows calculated frequencies. Some experimental frequencies can be located, but there are some additional frequencies not present in experimental data.

In the case of brucite with  $C2/m$  structure, with five atoms in the unit cell, there are 15 normal modes. According to group theory, the acoustic modes are  $A$  and  $2B$ . Six modes are infrared active ( $2A_u$  and  $4B_u$ ) and three modes are Raman active ( $4A_g$  and  $2B_g$ ). Calculated frequencies are shown in Table 2.

Fig. 4 shows calculated phonon dispersion curves for the three structures at 0 K. The  $P\bar{3}m1$  and  $P\bar{3}$  structures show the presence of unstable phonon modes:  $P\bar{3}m1$  around the  $k$  point and  $P\bar{3}$  along the  $\Gamma$ -A direction. While the  $C2/m$  structure does not show any phonon instability, which suggests that this structure could be considered as a better representation of the brucite system, at least at room temperature, where the quantum nature of the hydrogen bond is also reduced.

To assess the existence of different phases in  $Mg(OH)_2$ , we have calculated the Raman intensity peaks and compared them directly to our experimental measurements as described in the methods section. Fig. 5 summarizes our results. On one side, the experiment shows the  $E_g$ ,  $A_{2u}$  and  $A_{1g}$  peaks that are assigned to the symmetric structure and discussed in detail in ref. 38.  $A_{1g}$  is a symmetric stretch. The appearance of the  $A_{2u}$

peak corresponds to an IR active anti-symmetric stretch mode. While more symmetric bonds cause greater change in the Raman spectra, this antisymmetric mode can be observed in Raman as it is not fully antisymmetric (as it breaks the anti-symmetry). This peak should correspond to an order-disorder phase transition. On the other hand, a new peak on the left-hand side of  $A_{1g}$  was observed.<sup>38</sup> That is a peak that can not be assigned based on the perfect brucite structure. A similar peak is observed from our theoretical calculations, but the similarity between the different intensities does not allow us to distinguish the corresponding structure responsible for such a peak. What we can conclude is basically that the new peak should come from a distorted structure such as one of the ones we are proposing here.

### 3.3 Anharmonic vibrational analysis

The considerable freedom of the OH bonds in the  $Mg(OH)_2$  interlayer allows for extensive exploration of the potential energy surface by the hydrogens, opening the door to substantial anharmonic effects. Fig. 6 shows the relative displacement of the hydrogen atoms with respect to the closest magnesium atom projected on the layer plane at 300 K. These trajectories were used for the anharmonic thermal analysis discussed below. In this figure, the H atoms in the  $P\bar{3}m1$  structure show very long excursions around their equilibrium positions as a result of thermal agitation, with  $P\bar{3}$  coming next. For the case of  $P\bar{3}$ , the hydrogen displacement is more reduced parallel to the octahedral plane, but they explore more of the perpendicular

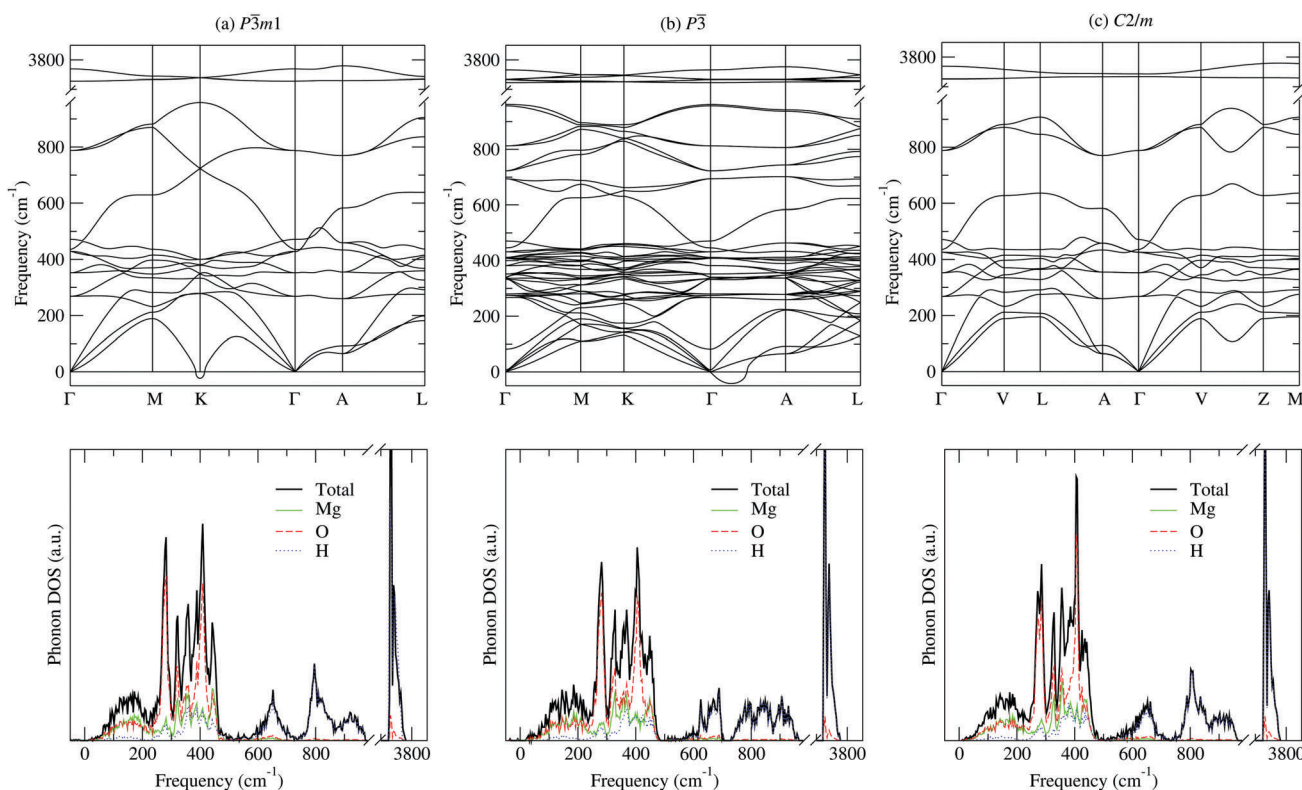


Fig. 4 Phonon spectrum and phonon density of states of (a)  $P\bar{3}m1$ , (b)  $P\bar{3}$  and (c)  $C2/m$  symmetries.

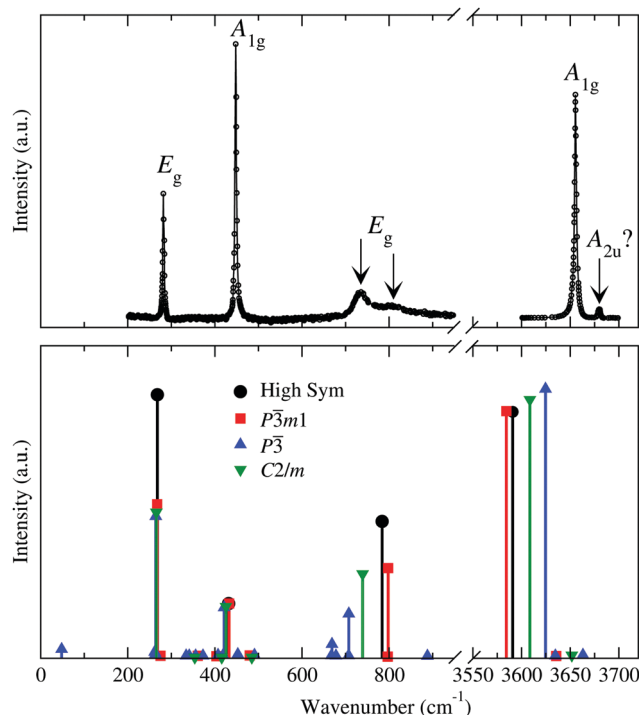


Fig. 5 Top: Experimental Raman spectra. Bottom: Theoretical Raman spectra for the  $P\bar{3}m1$ ,  $P\bar{3}$  and  $C2/m$  structures.

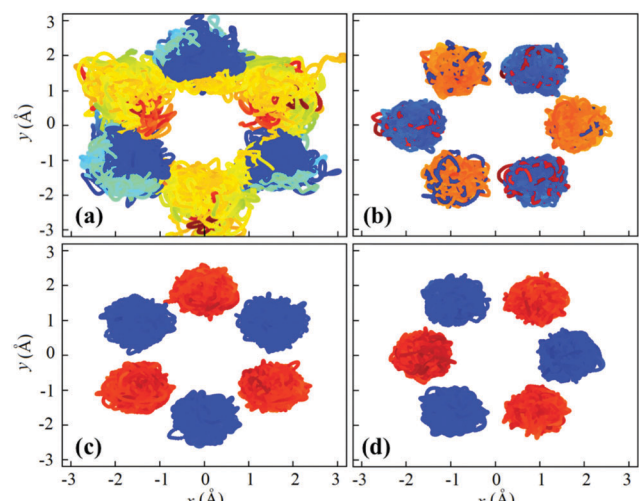


Fig. 6 Two-dimensional projection of the hydrogen displacement with respect to the ( $x, y$ ) magnesium position. (a)  $P\bar{3}m1$ , (b)  $P\bar{3}$ , (c)  $P\bar{3}m1$ , and (d)  $C2/m$  symmetries. Blue colors refer to the projection of the hydrogen displacement below the magnesium atoms while red colors correspond to those on top of the magnesium atoms. As the color deviates from red or blue, the dispersion of the displacement of hydrogens in the  $z$ -axis increases. Note that you can measure how far the hydrogens have moved on the  $x$ - and  $y$ -axes.

space, which might be correlated to a higher stretching frequency.  $C2/m$  and  $P\bar{3}m1$  show very similar behavior and the hydrogens are very well localized in the plane parallel to the layers. The mean square displacement also provides us with some information about the present anharmonicity. The larger the atomic

excursions from the equilibrium position the greater the deviation from a harmonic potential. The  $C2/m$  structure shows a more confined atomic displacement, which is the closest to harmonic behavior.

Fig. 7 shows calculated phonons for the three low-symmetry structures obtained from potential parameters fitted from the MD runs at 300 and 600 K. The results show that at room temperature,  $P\bar{3}m1$  is still unstable, with imaginary phonons close to the  $\Gamma$  point. With temperature all phonons soften except for the unstable mode whose energy increases and by 600 K it shows only positive frequencies. A similar situation is also observed for  $P\bar{3}$  but the negativity of the phonon branch is much smaller and it could be that at 300 K the structure becomes stable. The  $C2/m$  phase is different in that respect, it has phonons which are positive even at 300 K, which indicates that this phase is energetically and thermally stable at room temperature.

The flat dispersion along vertical lines in the Brillouin zone like XS or UR suggest weaker interactions between the layers. This weak dispersion is also seen in the thermal conductivity as in Fig. 8. The values indicate that perpendicular to the layers (the ZZ direction in this plot) the conductivity is very low, a typical behavior of layered materials (a short scattering length). On the other hand, the thermal conductivity in plane is anisotropic with values larger than magnesium hydroxide in bulk, which explains why this material enhances the thermal conductivity in composites.<sup>53–55</sup> The power law dependence of the thermal conductivity can also be extracted from our calculations, with a power law value of  $-2.2 \times 10^{-3}$ ,  $-2.1 \times 10^{-3}$  and  $-2.0 \times 10^{-3}$  along the  $a$ ,  $b$  and  $c$  crystallographic axis, respectively.

Our results indicate that at 300 K, there is a competition of different phases, which do not involve a change in the magnesium positions but involve changes in the hydrogen positions. This amorphization has been predicted before using constant pressure *ab initio* molecular dynamics.<sup>56</sup> This amorphization is very similar to our analysis on the hydrogen delocalization from Fig. 6.

As far as we know, this is the first time that the brucite structure is defined by considering the temperature dependence of phonon dispersion curves along the reciprocal space and not only at the  $\Gamma$  point; and therefore taking into account the direct temperature effect on the atomic vibrations and the potential seen by the ions. Thus, our calculations indicate that the real stabilization of the brucite  $P\bar{3}$  structure occurs when the temperature rises, even though this is a low temperature transition taking place at approximately 600 K. Our results confirm that at this temperature and even above this, all phonons have real values in the full reciprocal space. Even when phonons reveal a stable structure, it should be remembered that this structure does not reproduce exactly experimental IR and Raman spectra as mentioned in Table 2.

According to this, our calculations suggest  $C2/m$  as a more accurate representation of the brucite system when taking into account phonon stabilities, the resulting IR and Raman spectra, and the XRD diffraction pattern. The structure is very similar to  $P\bar{3}m1$  but the symmetry is decreased from space group 164 to 12.

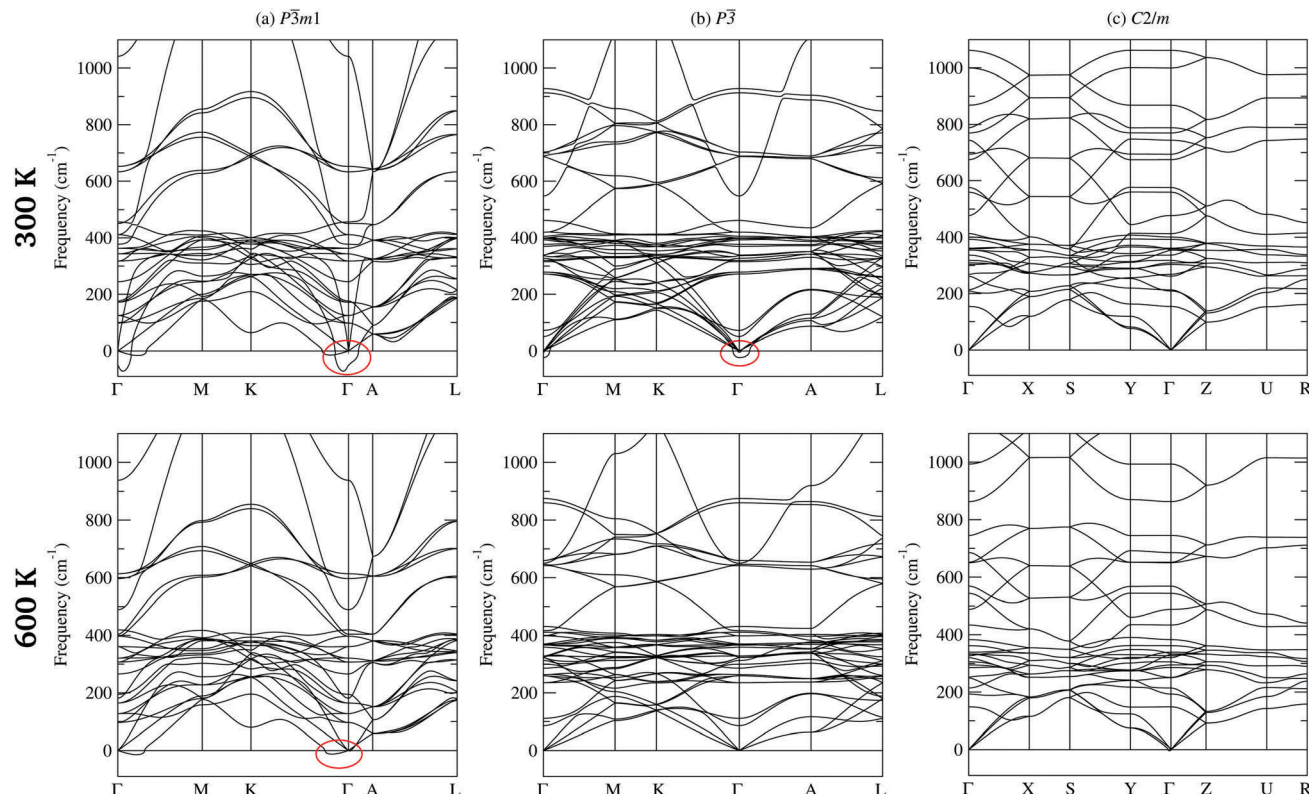


**Fig. 7** Calculated phonon dispersion curves for  $P\bar{3}m1$ ,  $P\bar{3}$ , and  $C2/m$  at 300 K (upper panels) and 600 K (lower panels). Figures show imaginary modes (red circles) denoting that the  $P\bar{3}m1$  and  $P\bar{3}$  structures are unstable at 300 K. When the temperature is increased to 600 K, the imaginary modes disappear for the  $P\bar{3}$  structure which means that it is stable at this condition. The  $C2/m$  structure does not exhibit imaginary modes even at 300 K while  $P\bar{3}m1$  does not stabilize even at 600 K.

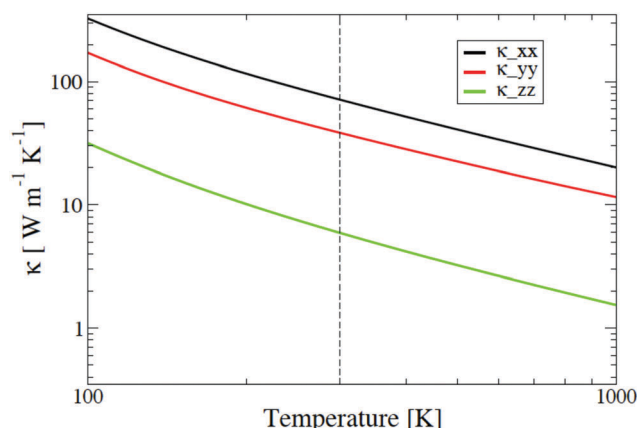


**Fig. 8** Calculated thermal conductivity for the  $C2/m$  phase.

## 4 Conclusions

Four possible structures were explored:  $C2/m$ ,  $P\bar{3}$ ,  $P3m1$  and  $P\bar{3}m1$ , where the last one is the currently accepted geometry in the literature. Energetics and the temperature dependence of phonon spectra allow us to discard the  $P3m1$  crystal phase. For the remaining three structures, it was shown that the structural distortions due to the different H ordering patterns are too small to be visible in XRD patterns.

We analyzed in detail the vibrational properties of the three lower symmetry structures. At 0 K, the  $P\bar{3}m1$  and  $P\bar{3}$  structures exhibit unstable phonon modes with imaginary frequencies. Calculations of the phonon spectra at finite temperature show that these instabilities persist up to at least 600 K for  $P\bar{3}m1$  and up to at least 300 K for  $P\bar{3}$ . The  $C2/m$  structure is dynamically stable.

The analysis of the Raman spectra, and the comparison between experiment and calculations suggest that the several extra peaks in the experimental spectra recorded at liquid nitrogen temperature are the result of ordering of hydrogen on a lower-symmetry lattice, like the one found in the  $C2/m$  structure.

The analysis of the trajectories of the H atoms during vibrations at 300 K and 600 K shows that H atoms explore a wide space region extending both parallel to the octahedral planes, but also in the interlayer space.

But the actual structure of brucite at low temperature can be a mixture of several low-symmetry phases, from which  $C2/m$  is a promising example. Moreover, the final answer concerning the behavior of H atoms will be obtained only when simulations take into account the complete quantum nature of hydrogen.

## Conflicts of interest

There are no conflicts to declare.

## Acknowledgements

P. Treviño thanks CONACYT for the financial support that was provided for her PhD studies. Support from Conacyt project 152153 is also recognized. A. H. R. acknowledge the support of NSF under grants 1434897, 1740111 and DOE under grant DOE DE-SC0016176. S. L.-M. thanks CONACYT of Mexico for financial support through the program “Cátedras para Jóvenes Investigadores”. The authors gratefully acknowledge the computing time granted by LANCASTER and CONACYT on the supercomputer Miztli at LSVP DGTIC UNAM. Also, some of the computing for this project was performed with the resources of the IPICYT Supercomputing National Center for Education & Research, grant TKII-R2018-SLM1. We acknowledge the support from the Extreme Science and Engineering Discovery Environment (XSEDE), an organization that is supported by the National Science Foundation Grant No. ACI-1053575, the supercomputer Stampede at the University of Texas, the Bridges supercomputer at the Pittsburgh supercomputer center, and the Occigen supercomputer at CINES through eDARI computational grant A0011006368.

## References

- 1 C. Y. Tai, C.-T. Tai, M.-H. Chang and H.-S. Liu, *Ind. Eng. Chem. Res.*, 2007, **46**, 5536–5541.
- 2 J. C. Yu, A. Xu, L. Zhang, R. Song and L. Wu, *J. Phys. Chem. B*, 2004, **108**, 64–70.
- 3 W. Fan, S. Sun, L. You, G. Cao, X. Song, W. Zhang and H. Yu, *J. Mater. Chem.*, 2003, **13**, 3062–3065.
- 4 F. Zigan and R. Rothbauer, *Neues Jahrb. Miner. Monatshefte*, 1967, **137**, 4–5.
- 5 P. Baranek, A. Lichanot, R. Orlando and R. Dovesi, *Chem. Phys. Lett.*, 2001, **340**, 362–369.
- 6 F. Pascale, S. Tosoni, C. Zicovich-Wilson, P. Ugliengo, R. Orlando and R. Dovesi, *Chem. Phys. Lett.*, 2004, **396**, 308–315.
- 7 L. Desgranges, G. Calvarin and G. Chevrier, *Acta Crystallogr. Sect. B: Struct. Sci.*, 1996, **52**, 82–86.
- 8 J. B. Parise, K. Leinenweber and D. J. Weidner, *Am. Mineralogist*, 1994, **79**, 193–196.
- 9 T. S. Duffy, C. Meade and Y. Fei, *Am. Mineralogist*, 1995, **80**, 222–230.
- 10 M. B. Kruger, Q. Williams and R. Jeanloz, *J. Chem. Phys.*, 1989, **91**, 5910–5915.
- 11 D. E. Partin, M. O'Keefe and R. B. Von Dreele, *J. Appl. Crystallogr.*, 1994, **27**, 581–584.
- 12 M. Catti, G. Ferraris, S. Hull and A. Pavese, *Phys. Chem. Miner.*, 1995, **22**, 200–206.
- 13 P. T. Jochym, A. M. Oles, K. Parlinski, J. Lazewski, P. Piekarz and M. Sternik, *J. Phys.: Condens. Matter*, 2010, **22**, 445403.
- 14 D. M. Sherman, *Am. Mineralogist*, 1991, **76**, 1769–1772.
- 15 P. D'Arco, M. Causà, C. Roetti and B. Silvi, *Phys. Rev. B: Condens. Matter Mater. Phys.*, 1993, **47**, 3522–3529.
- 16 M. Mookherjee and L. Stixrude, *Am. Mineralogist*, 2006, **91**, 127.
- 17 G. Kresse and J. Furthmüller, *Phys. Rev. B: Condens. Matter Mater. Phys.*, 1996, **54**, 11169–11186.
- 18 G. Kresse and D. Joubert, *Phys. Rev. B: Condens. Matter Mater. Phys.*, 1999, **59**, 1758–1775.
- 19 P. E. Blöchl, *Phys. Rev. B: Condens. Matter Mater. Phys.*, 1994, **50**, 17953–17979.
- 20 J. P. Perdew, A. Ruzsinszky, G. I. Csonka, O. A. Vydrov, G. E. Scuseria, L. A. Constantin, X. Zhou and K. Burke, *Phys. Rev. Lett.*, 2008, **100**, 136406.
- 21 H. J. Monkhorst and J. D. Pack, *Phys. Rev. B: Solid State*, 1976, **13**, 5188–5192.
- 22 S. Baroni, S. De Gironcoli, A. Dal Corso and P. Giannozzi, *Rev. Mod. Phys.*, 2001, **73**, 515.
- 23 A. Togo, F. Oba and I. Tanaka, *Phys. Rev. B: Condens. Matter Mater. Phys.*, 2008, **78**, 134106.
- 24 K. Parlinski, Computer Code PHONON, see: <http://wolf.ifj.edu.pl/phonon>.
- 25 S. López-Moreno, A. H. Romero, J. Mejía-López and A. Muñoz, *Phys. Chem. Chem. Phys.*, 2016, **18**, 33250–33263.
- 26 S. López-Moreno, A. H. Romero, J. Mejía-López, A. Muñoz and I. V. Roshchin, *Phys. Rev. B: Condens. Matter Mater. Phys.*, 2012, **85**, 134110.
- 27 J. A. Barreda-Agüeso, S. López-Moreno, M. N. Sanz-Ortiz, F. Aguado, R. Valiente, J. González, F. Rodríguez, A. H. Romero, A. Muñoz, L. Nataf and F. Baudelet, *Phys. Rev. B: Condens. Matter Mater. Phys.*, 2013, **88**, 214108.
- 28 X. Gonze, G.-M. Rignanese and R. Caracas, *Z. Kristallogr. – Cryst. Mater.*, 2005, **220**, 458–472.
- 29 M. Veithen, X. Gonze and P. Ghosez, *Phys. Rev. B: Condens. Matter Mater. Phys.*, 2005, **71**, 125107.
- 30 X. Gonze, F. Jollet, F. A. Araujo, D. Adams, B. Amadon, T. Applencourt, C. Audouze, J.-M. Beuken, J. Bieder, A. Bokhanchuk, E. Bousquet, F. Bruneval, D. Caliste, M. Cote, F. Dahm, F. D. Pieve, M. Delaveau, M. D. Gennar, B. Dorado, C. Espejo, G. Geneste, L. Genovese, A. Gerossier, M. Giantomassi, Y. Gillet, D. R. Hamann, L. He, G. Jomard, J. L. Janssen, S. L. Roux, A. Levitt, A. Lherbier, F. Liu, I. Lukacevic, A. Martin, C. Martins, M. J. T. Oliveira, S. Ponce, Y. Pouillon, T. Rangel, G.-M. Rignanese, A. H. Romero, B. Rousseau, O. Rubel, A. A. Shukri, M. Stankovski, M. Torrent, M. J. V. Setten, B. V. Troeye, M. J. Verstraete, D. Waroquier, J. Wiktor, B. Xue, A. Zhou and J. W. Zwanziger, *Comput. Phys. Commun.*, 2016, **205**, 106.
- 31 X. Gonze, G. Rignanese, M. Verstraete, J. Betiken, Y. Pouillon, R. Caracas, F. Jollet, M. Torrent, G. Zerah, M. Mikami, P. Ghosez, M. Veithen, J.-Y. Raty, V. Olevano, F. Bruneval, L. Reining, R. Godby, G. Onida, D. Hamann and D. Allan, *Z. Kristallogr.*, 2005, **220**, 558–562.
- 32 M. Fuchs and M. Scheffler, *Comput. Phys. Commun.*, 1999, **119**, 67–98.
- 33 R. Caracas and E. Bobocioiu, *Am. Mineralogist*, 2011, **96**, 437–443.
- 34 O. Hellman, P. Steneteg, I. A. Abrikosov and S. I. Simak, *Phys. Rev. B: Condens. Matter Mater. Phys.*, 2013, **87**, 104111.
- 35 O. Hellman and I. A. Abrikosov, *Phys. Rev. B: Condens. Matter Mater. Phys.*, 2013, **88**, 144301.
- 36 S. Nosé, *Mol. Phys.*, 1984, **52**, 255–268.
- 37 W. G. Hoover, *Phys. Rev. A: At., Mol., Opt. Phys.*, 1985, **31**, 1695.
- 38 B. Reynard and R. Caracas, *Chem. Geol.*, 2009, **262**, 159–168.

- 39 Y. Fei and H.-K. Mao, *J. Geophys. Res.: Solid Earth*, 1993, **98**, 11875–11884.
- 40 S. A. T. Redfern and B. J. Wood, *Am. Mineralogist*, 1992, **77**, 1129.
- 41 H. Fukui, O. Ohtaka, T. Suzuki and K. Funakoshi, *Phys. Chem. Miner.*, 2003, **30**, 511–516.
- 42 X. Xia, D. J. Weidner and H. Zhao, *Am. Mineralogist*, 1998, **83**, 68–74.
- 43 D.-Y. Zhang, P. Yang, Z. Du, Q.-H. Yuan, S.-H. Song, X.-Z. Ren and P.-X. Zhang, *Trans. Nonferrous Met. Soc. China*, 2015, **25**, 4080–4088.
- 44 B. Winkler, V. Milman, B. Hennion, M. C. Payne, M.-H. Lee and J. S. Lin, *Phys. Chem. Miner.*, 1995, **22**, 461–467.
- 45 V. S. Vaiss, R. A. Berg, A. R. Ferreira, I. Borges and A. A. Leitao, *J. Phys. Chem. A*, 2009, **113**, 6494–6499.
- 46 K. Hermansson, M. M. Probst, G. Gajewski and P. D. Mitev, *J. Chem. Phys.*, 2009, **131**, 244517.
- 47 A. Pishtshev, S. Z. Karazhanov and M. Klopov, *Comput. Mater. Sci.*, 2014, **95**, 693–705.
- 48 A. Hermann and M. Mookherjee, *Proc. Natl. Acad. Sci. U. S. A.*, 2016, **113**, 13971–13976.
- 49 D. Zhang, P. Zhang, S. Song, Q. Yuan, P. Yang and X. Ren, *J. Alloys Compd.*, 2014, **612**, 315–322.
- 50 P. Dawson, C. Hadfield and G. Wilkinson, *J. Phys. Chem. Solids*, 1973, **34**, 1217–1225.
- 51 H. Lutz, *Coordination Chemistry*, Springer Berlin Heidelberg, 1995, vol. 82, pp. 85–103.
- 52 R. L. Frost and J. T. Kloprogge, *Spectrochim. Acta, Part A*, 1999, **55**, 2195–2205.
- 53 C. C. Knight, F. Ip, C. Zeng, C. Zhang and B. Wang, *Fire Mater.*, 2013, **37**, 91–99.
- 54 S.-P. Liu, J.-R. Ying, X.-P. Zhou, X.-L. Xie and Y.-W. Mai, *Compos. Sci. Technol.*, 2009, **69**, 1873–1879.
- 55 H. Huang, M. Tian, L. Liu, W. Liang and L. Zhang, *J. Appl. Polym. Sci.*, 2006, **100**, 4461–4469.
- 56 S. Raugei, P. L. Silvestrelli and M. Parrinello, *Phys. Rev. Lett.*, 1999, **83**, 2222–2225.